Phase Behavior and Adsorption of Pure Substances and Mixtures and Characterization in Nanopore Structures by Density Functional Theory

Zhidong Li, SPE, and **Zhehui Jin,** Reservoir Engineering Research Institute; and
Abbas Firoozabadi, SPE, Reservoir Engineering Research Institute and Yale University

Summary

Phase behavior in shale remains a mystery because of various complexities and effects. One complexity is from nanopores, in which phase behavior is significantly affected by the interaction between the pore surfaces and fluid molecules. The result is the heterogeneous distribution of molecules that cannot be described by bulk-phase thermodynamic approaches. Statistical thermodynamic methods can describe the phase behavior in nanopores. In this work, we apply an engineering density functional theory (DFT) combined with the Peng-Robinson equation of state (EOS) to investigate the adsorption and phase behavior of pure substances and mixtures in nanopores, and include the characterization of pore structure of porous media. The nanopores are represented by carbon-slit pores each consisting of two parallel planar-infinite structureless graphite surfaces. The porous media are activated carbons and dry coal, each modeled by an array of polydisperse carbon-slit pores. We study the influence of multiple factors on phase transitions of various pure light species and their mixtures in nanopores. We find that capillary condensation and hysteresis are more likely in heavier hydrocarbons, at lower temperatures, and in smaller pores. For pure hydrocarbons in nanopores, the phase change always occurs below the critical temperature and saturation pressure. For mixtures in nanopores, there may be a phase change above the cricondentherm. We characterize the pore structure of porous media to obtain the pore-size distribution (PSD), surface area (SA), and pore volume (PV) on the basis of the measured adsorption isotherms of pure substances. Then, we use the computed PSD to predict the adsorption of mixtures in porous media. There is agreement between the experiments and our predictions. This work is in the direction of phase-behavior modeling and understanding in shale media.

Introduction

Shale gas and shale light oil have had a game-changing impact in hydrocarbon production in the past few years. To predict the well productivity of shale reservoirs, the knowledge of phase behavior and fluid flow of hydrocarbons is key. Phase behavior in shale gas and shale light-oil reservoirs is dramatically different from that in conventional reservoirs and tight gas and oil reservoirs. One complexity is from the dual nature of shale permeable media. In conventional reservoirs and tight reservoirs, the oil and gas are the only organic matter. In shale reservoirs, the organic matter also constitutes a portion of the rock in solid form (kerogen). The other portion of the shale rock is inorganic matter, such as clay. Another complexity is from the nanopores widely distributed in both organic and inorganic matter. Nanopores may result in a large share of adsorption of hydrocarbon molecules in relation to the total (Montgomery et al. 2005). The phase behavior becomes very complex in shale reservoirs because of multiple effects. In a number of shale light-oil reservoirs, the sampled fluids are strongly undersaturated, but the gas/oil ratio increases significantly at the early stage of production. In conventional reservoirs, the gas/oil ratio will stay constant until the reservoir pressure drops below the saturation pressure. To understand the phase behavior in shale reservoirs, we need to understand the phase behavior in both organic and inorganic portions of the shale, which is tied to the phase behavior in nanopores and some other complexities depending on the type of organic and inorganic matter. In this work, the focus is on the phase behavior in nanopores. In future publications, other complexities of the organic and inorganic matter will be introduced. The ultimate goal of our work is to describe the phase behavior in shale reservoirs.

The phase behavior (defined in terms of adsorption and phase transitions) of pure substances and mixtures in very-small pores, with size of a few molecule diameters, is of fundamental importance for many industrial and geophysical operations besides shale gas and shale light oil. Fluids confined within small pores may exhibit a wide range of phase behavior. The introduction of surface forces and the competition between fluid/surface and fluid/fluid interactions may lead to the heterogeneous distribution of fluid molecules in small pores. Various surface-driven phase transitions are significantly different from those in the bulk. For instance, a fluid near a single solid surface may give rise to the intricate prewetting and wetting transitions (Gelb et al. 1999). The behavior becomes even more complicated in small pores because some characteristic measures of confinement (such as pore size, geometry, and chemistry of solid surface) may result in diverse transitions such as layering and capillary condensation. Phase transition may be more complicated in nanopores than in large pores because the surface molecules can influence the fluid molecules in the whole pore space. Adsorption and desorption sometimes do not follow the same path. Hysteresis in adsorption and desorption can be interpreted in terms of thermodynamic metastability, where the system is trapped in a local free-energy minimum (Gelb et al. 1999). The adsorbed molecules (more precisely, the stronger fluid/surface interaction over fluid/fluid interaction near the surface) contribute mainly to the hysteresis. Hysteresis may have a large effect on hydrocarbon production in shale reservoirs because both organic matter and inorganic matter demonstrate a wide range of pore sizes from less than one to tens of nanometers.

Adsorption in porous media depends on bulk pressure, temperature, PV, surface area, PSD, and pore chemistry. In this work, we do not consider different pore chemistries important in shale media. The pores are classified as micropores with sizes smaller than 2 nm, mesopores with sizes between 2 and 50 nm, and macropores with sizes greater than 50 nm, according to the International Union of Pure and Applied Chemistry. In the characterization of a porous medium, typically nitrogen (N_2) adsorption/desorption isotherms are measured at 77 K to the saturation pressure. At saturation pressure, the gas condenses to liquid in the pores completely. The adsorbed amounts and capillary condensation/evaporation pressures are related to the geometrical properties of the porous medium. The specific surface area is usually assessed from the adsorption

Copyright © 2014 Society of Petroleum Engineers

Original SPE manuscript received for review 24 October 2012. Revised manuscript received for review 10 February 2014. Paper (SPE 169819) peer approved 19 February 2014.

experiments before the capillary condensation on the basis of the Brunnauer-Emmet-Teller (BET) method of multilayer adsorption. By assuming that the pore surface is completely and uniformly covered by the fluid molecules, the surface area is estimated from the number of fluid molecules in the first layer and the area occupied by each fluid molecule (Brunauer et al. 1938; Roque-Malherbe 2007). The *t*-plot method establishes the relation between the thickness of multilayer adsorption *t* and adsorbed amount to estimate the volume of micropores and the surface area excluding the micropores (Halsey 1948; Roque-Malherbe et al. 2007). The Barret-Joyner-Hallenda (BJH) method is used to determine the PSD in the mesopore range from the desorption data on the basis of the Kelvin equation, which describes the relation between the pore size and condensation pressure. At the initial pressure of desorption, all the pores are filled with liquid. As the pressure drops, desorption evolves from the vaporization of the condensed phase in smaller pores and thinning of the adsorption layer in larger pores where the condensed phase has already been removed (Cohan 1938; Barret et al. 1951; Roque-Malherbe 2007). These techniques may have limitations. The BET, *t*-plot, and BJH methods are all based on multilayer adsorption. The BET method may be inaccurate for micropores because multiple adsorption layers may not form. The BJH method may have a large error for micropores because the Kelvin equation may not be valid (Adesida et al. 2011; Kuila and Prasad 2011).

There has been gradual progress in estimating mixture adsorption in porous media comprising nanopores. The benchmark is the "ideal adsorbed solution theory" by Myers and Prausnitz (1965). This method does not require modeling of the adsorbent or the adsorbates; its performance deteriorates for increasingly nonideal systems (Sweatman and Quirke 2002). The nonideal behavior from the interaction between fluid molecules could be described by adopting different approximations. Traditional approaches such as the Langmuir and BET methods have also been applied to study the adsorption of mixtures in porous media (Langmuir 1916; Halsey 1948; Roque-Malherbe 2007). Qiao et al. (2000) and Dreibach et al. (1999) applied the extended Langmuir model to correlate the adsorption isotherms of pure substances in activated carbon and to determine the model parameters. The parameters are then used to predict adsorption of binary and ternary mixtures in the same activated carbon (Dreibach et al. 1999; Qiao et al. 2000). Despite the fact that the agreement between computations and data was satisfactory, because of a large number of parameters, these methods are unlikely to be efficient for the analysis of adsorption of various fluids in different porous media with a wide range of pore sizes. These methods require the knowledge of adsorption in porous media a priori. The Langmuir model is derived under the assumption that the fluid molecules form only one adsorption layer near the solid surface and in the rest of the domain the fluid is homogeneous (that is, the bulk). This is not the case in nanopores, as we see clearly in this work. The BET model is derived under the assumption that the fluid molecules form a possibly infinite number of adsorption layers near the solid surface. The use of the Langmuir and BET models is based on the empirical parameters that are obtained through matching the adsorption data. The parameters do not have generality because they must be adjusted for different fluids and different porous media. The extension of these methods to mixtures is not straightforward. There is need for additional approximations and adjustable parameters.

The more theoretically sophisticated local-density theories (Rangarajan et al. 1995; Subramanian et al. 1995) use an EOS modified for confined fluids. In principle, the behavior of confined-fluid phase is obtained by equaling the chemical potentials of bulk and adsorbed phase, which is described by the EOS and fluid/solid potential (Ustinov and Do 2003). Shapiro and Stenby (1998) and Monsalvo and Shapiro (2007; 2009a, 2009b) developed a multicomponent potential theory of adsorption (MPTA) to study mixture adsorption in porous materials. The key idea of MPTA is that chemical potential of a component in a mixture is contributed by a bulk phase described by EOS and a potential-energy contribution depending on the distance to the adsorbent (Monsalvo and Shapiro 2007). With simple assumption of adsorption potential and adjustable parameters, MPTA shows good agreement with experimental data in multicomponent adsorption in porous media [Shapiro and Stenby (1998); Monsalvo and Shapiro (2007; 2009a,2009b)]. Although the properties of adsorbates can be described by an EOS in macropores; the properties in micropores (<2 nm) are completely different from those in the bulk. In micropores, statistical thermodynamics from the molecular perspective is necessary (Monsalvo and Shapiro 2007). The MPTA approach may not describe the hysteresis process.

The DFT and grand canonical Monte Carlo (GCMC) simulation have been widely adopted to study adsorption and phase behavior of fluids in small pores and in porous media (Gelb et al. 1999). These statistical thermodynamic approaches are based on the description of fluid/fluid and fluid/surface interactions and connect the heterogeneous molecular distributions in a pore to the macroscopic properties. They are applicable both to pure substances and to mixtures. There is no need to assume monolayer or multilayer adsorption a priori. GCMC simulation can account for more details of molecular structures; DFT is computationally much more efficient. The equilibrium-density profiles are obtained by minimizing the grand potential in DFT. Because DFT considers nonlocal behavior of structural and thermodynamic properties, it can be used to study complicated problems such as interfacial phenomena and phase transition. Many versions of DFT have been applied to study adsorption of fluids in small pores and in porous media. The past work is based on the use of the statistical associating fluid theory (SAFT) and its analogs (Chapman et al. 1988; Chapman et al. 1989; Chapman et al. 1990). SAFT is not the best choice in describing hydrocarbon fluids because conventional cubic EOSs have higher accuracy and less mathematical complexity. The DFT study of mixture adsorption in porous media is very limited. Ottiger et al. (2008a) have applied a lattice DFT to study the adsorption of pure substances and mixtures consisting of N_2, methane, and carbon dioxide (CO_2) in a dry coal. Although this model can reproduce the adsorption isotherms, it introduces many assumptions, has complicated formalism, and contains a large number of adjustable parameters.

The Peng-Robinson EOS (PR-EOS) (Peng and Robinson 1976; Robinson et al. 1985) can accurately describe the phase behavior and thermodynamic properties of bulk hydrocarbon fluids. It has been successfully applied to numerous hydrocarbon-reservoir fluids. Encouraged by its excellent performance in relation to bulk-phase description, recently we have proposed an engineering version of DFT to extend the PR-EOS from the bulk to the heterogeneous condition where molecular distribution is not uniform (Li and Firoozabadi 2009). We use the weighted-density approximation (Rosenfeld 1989) and quadratic-density expansion (Ebner et al. 1976; Ebner and Saam 1977) to make the extension from homogeneous to heterogeneous conditions. Its validity has been confirmed by accurate prediction of interfacial tension of pure substances and binary mixtures. The SAFT-based DFT cannot describe both bulk and interfacial properties simultaneously using the same set of parameters, which leads to thermodynamic inconsistency.

In this work, we adopt our engineering DFT to study the adsorption and phase behavior of pure substances and their mixtures in nanopores and in porous media consisting of nanopores. We first investigate the influence of species, temperature, and pore size on adsorption and capillary condensation of pure hydrocarbons and mixtures in carbon-slit nanopores. The investigation establishes a basic knowledge on phase transitions of fluids in very small pores. Then, we study the adsorption of fluids in well-defined carbonaceous porous media; that is, activated carbons and dry coal. We use the adsorption isotherms of pure substances in a porous medium to obtain a unique PSD. In the past, the computed PSD has not been found to be unique for a given porous medium. Adopting different methods and correlating different adsorption isotherms have produced different PSDs (Sweatman and Quirke 2001). However, the PSD is an intrinsic property of a porous medium and should not vary for a given sample. We use the unique PSD from adsorption isotherms of pure substances to predict the

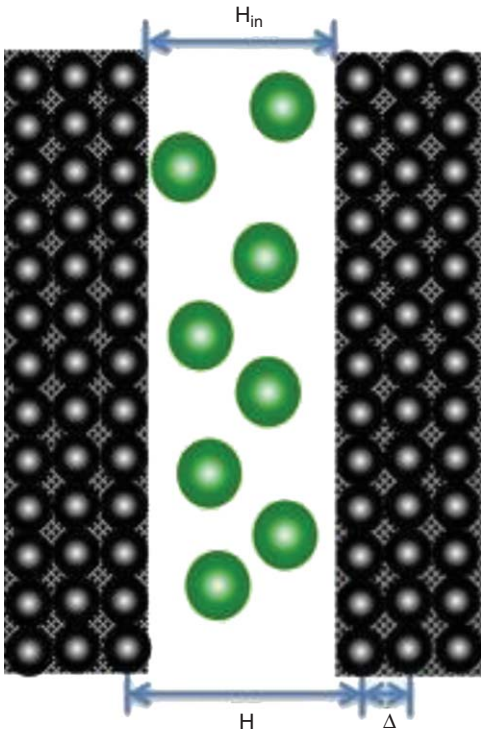

Fig. 1—Molecular model of fluid in a carbon-slit pore. Black and green spheres represent carbon atoms and fluid molecules, respectively (Ravikovitch 2000).

adsorption of binary and ternary mixtures in the same porous medium. There is agreement between our predictions and measurements. Compared with the alternative methods, especially the lattice DFT by Ottiger et al. (2008a), our DFT has an EOS foundation, much simpler formalism, only one adjustable parameter, and broader applications.

The remainder of this article is organized as follows. We first present a very brief formulation of our DFT and describe how to obtain the only unknown parameter to complete the theory. Then, we examine the adsorption and desorption of pure hydrocarbons and mixtures in single carbon-slit pores and discuss how our results can explain some aspects of phase behavior in shale. Next, we use the adsorption data of both pure substances and mixtures in three activated carbons and dry coal to systematically examine the performance of our theory. At the end, the main results and conclusions are summarized. Appendix A provides a brief theoretical background for the classical DFT.

Basic Formalism

In a nanopore, the fluid molecules are heterogeneously distributed because of the position-dependent fluid/surface interactions and the competition between fluid/fluid and fluid/surface interactions. DFT constructs the free energy depending on different approximations and expresses it as functional of heterogeneous molecular distributions to describe the fluid/fluid and fluid/surface interactions. The equilibrium molecular distributions are computed at the minimum of the free energy, and then macroscopic properties, such as adsorption amount, are readily computed.

The problem is formulated in terms of species distributions in a nanopore linked to the outside (or bulk) where the composition, temperature, and pressure are fixed (i.e., the fluid in the nanopore constitutes an open system). The temperature in the nanopore is identical to that in the outside. The volume of the nanopore is fixed. It is different from a closed system (specified by constant temperature, volume or pressure, and number of molecules) that has only energy exchange with the bulk through a solid boundary, and uses the Helmholtz energy or Gibbs energy as the thermodynamic function. An open system (specified by constant temperature, volume, and chemical potentials) has both energy and mass exchange with the bulk through an imaginary boundary, and the grand potential is the thermodynamic function of choice. The grand potential functional $\Omega\{[\rho_k(\mathbf{r})]\}$ is related to the Helmholtz free-energy functional $F\{[\rho_k(\mathbf{r})]\}$ by the Legendre transformation,

$$\Omega\{[\rho_k(\mathbf{r})]\} = F\{[\rho_k(\mathbf{r})]\} + \sum_k \int d\mathbf{r}\rho_k(\mathbf{r})[\Psi_k(\mathbf{r}) - \mu_k], \quad \cdots\cdots\cdots\cdots\cdots\cdots (1)$$

where d$\mathbf{r}$ is the differential volume, $\rho_k(\mathbf{r})$ is the number density distribution of component k at position $\mathbf{r}$, $\Psi_k(\mathbf{r})$ is the external potential of component k at position $\mathbf{r}$ from the solid surface, and μ_k is the chemical potential of component k. The Helmholtz free-energy functional $F\{[\rho_k(\mathbf{r})]\}$ can be further decomposed into the ideal-gas term without the intermolecular interactions and the excess term accounting for the intermolecular interactions leading to the thermodynamic nonideality:

$$F\{[\rho_k(\mathbf{r})]\} = F^{\mathrm{id}}\{[\rho_k(\mathbf{r})]\} + F^{\mathrm{ex}}\{[\rho_k(\mathbf{r})]\}. \quad \cdots\cdots\cdots (2)$$

$F^{\mathrm{id}}\{[\rho_k(\mathbf{r})]\}$ is known exactly. $F^{\mathrm{ex}}\{[\rho_k(\mathbf{r})]\}$ is formulated approximately. In our engineering DFT, $F^{\mathrm{ex}}\{[\rho_k(\mathbf{r})]\}$ consists of two parts. The first part is extended from the PR-EOS (Peng and Robinson 1976; Robinson et al. 1985) by adopting the weighted-density approximation (Rosenfeld 1989). The second part is supplemented by the quadratic density expansion (Ebner et al. 1976; Ebner and Saam 1977) and vanishes in the bulk. The details are provided in our article (Li and Firoozabadi 2009) and are not repeated, for the sake of brevity. At local or global minimum of $\Omega\{[\rho_k(\mathbf{r})]\}$, its functional derivative is zero; that is, $\delta\Omega/\delta\rho_k(\mathbf{r}) = 0$. Equivalently, the chemical potential of each component in the nanopore is identical to that in the bulk phase outside; that is, $\mu_k = \Psi_k(\mathbf{r}) + \delta F/\delta\rho_k(\mathbf{r})$ (Eq. A-6 in Appendix A is for a single-component system), and the equilibrium-density distributions satisfy

$$\rho_k(\mathbf{r}) = \exp\left[\beta\mu_k - \beta\Psi_k(\mathbf{r}) - \frac{\delta\beta F^{\mathrm{ex}}}{\delta\rho_k(\mathbf{r})}\right], \quad \cdots\cdots\cdots\cdots (3)$$

where $\beta = 1/(k_B T)$, with k_B and T being the Boltzmann constant and absolute temperature, respectively.

Activated carbons can be represented by a polydisperse array of carbon-slit pores when using DFT and GCMC (Ravikovitch et al. 2000). This model is also considered to be a good approximation to the nature of kerogen pores in shale (Adesida et al. 2011; Kuila and Prasad 2011). In a slit pore, the density distributions vary only in the z-direction perpendicular to the solid surfaces; that is, $\rho_k(\mathbf{r}) = \rho_k(z)$. We assume the solid surface to be a planar-structureless graphite wall, as shown in **Fig. 1** (Ravikovitch et al. 2000). The interaction between the surface and component k is described by the Steele 10-4-3 potential (Steele 1973),

$$U_{sk}(z) = 2\pi\rho_s\varepsilon_{sk}\sigma_{sk}^2\Delta\left[\frac{2}{5}\left(\frac{\sigma_{sk}}{z}\right)^{10} - \left(\frac{\sigma_{sk}}{z}\right)^4 - \frac{\sigma_{sk}^4}{3\Delta(0.61\Delta + z)^3}\right], \quad \cdots\cdots\cdots\cdots\cdots\cdots (4)$$

where ρ_s=0.114 Å^{-3} is the density of graphite and Δ=3.35 Å is the interlayer spacing of graphite. ε_{sk} and σ_{sk} are estimated from the simple mixing rules: $\varepsilon_{sk} = \sqrt{\varepsilon_s\varepsilon_k}$, and $\sigma_{sk} = (\sigma_s + \sigma_k)/2$. σ_k is the "molecular diameter" of component k and can be calculated from its volume parameter of the PR-EOS (Li and Firoozabadi 2009). We assume the diameter of surface molecules σ_s to be 3.345 Å, as used by Olivier (1995). ε_k is the attraction-energy parameter of component k (Li and Firoozabadi 2009). ε_s is the attraction-energy parameter of surface molecules. The external potential for component k is expressed as $\Psi_k(z) = U_{sk}(z)$ near a single graphite surface or as $\Psi_k(z) = U_{sk}(z) + U_{sk}(H - z)$ in a carbon-slit pore. H is the apparent size of the slit pore. The inner (or effective) pore size is $H_{\mathrm{in}} = H - \sigma_s$.

TABLE 1—CRITICAL TEMPERATURE T_c, CRITICAL PRESSURE P_c, ACENTRIC FACTOR ω, MOLAR WEIGHT M_w, VOLUME SHIFT PARAMETER (VSP), and ATTRACTION ENERGY ε FOR DIFFERENT SPECIES

Species	T_c (K)	P_c (MPa)	ω	M_w (g/mol)	VSP	ε/k_B (K)
N_2	126.21	3.390	0.039	28.01	−0.16562	700
CO_2	304.14	7.375	0.239	44.01	−0.06225	1,760
C_1	190.56	4.599	0.011	16.04	−0.1533	1,178
C_2	305.32	4.872	0.099	30.07	−0.1094	1,540
C_3	369.83	4.248	0.153	44.10	−0.0869	1,866
n-C_4	425.12	3.796	0.199	58.12	−0.0672	2,236
n-C_5	469.70	3.370	0.251	72.15	−0.03865	2,517

We adopt a modified successive-substitution iteration to update the density distributions by linearly combining the input and output of Eq. 3 as a new input. It is a decent method, and the solution of Eq. 3 is at least a local minimum of Ω. The calculation of an isotherm is started at a sufficiently low pressure and ended at a sufficiently high pressure in the adsorption process (or vice versa in the desorption process) where Ω only has the global minimum. At the first pressure in the adsorption process where the initial guess is not available, the bulk density is used for the initialization. The solution of density distributions at other pressures uses the results at the preceding pressure as the initial guess in both adsorption and desorption processes, and Ω may converge to a local minimum if it exists. The calculation of adsorption and desorption isotherms simulates the real experimental procedure. As in the PR-EOS (Jhaveri and Youngren 1988), we introduce the volume translation to correct the equilibrium-density distribution calculated from Eq. 3.

Tables 1 and 2 provide the fluid parameters. In the PR-EOS with the volume translation, for each component, the critical temperature T_c, critical pressure P_c, acentric factor ω, and molar weight M_w are known, and dimensionless volume shift parameter (VSP) is obtained from fitting the equilibrium liquid density at T/T_c=0.7; between any two components, the binary interaction coefficient k_{ij} is the same as that used by Firoozabadi (1999). In the DFT, besides these parameters, for each component, the attraction-energy parameter ε is provided by Li and Firoozabadi (2009). The only unknown is the attraction-energy parameter of surface molecules ε_s, which is determined by fitting the adsorption isotherm of N_2 in Sterling graphite at 77.3 K (Olivier 1995; Ravikovitch et al. 2000). The excess adsorption per unit surface area

TABLE 2—BINARY INTERACTION COEFFICIENT k_{ij} BETWEEN ANY TWO SPECIES

N_2	0	—	—	—	—	—	—
CO_2	0	0	—	—	—	—	—
C_1	0.1	0.15	0	—	—	—	—
C_2	0.1	0.15	0.034	0	—	—	—
C_3	0.1	0.15	0.036	0	0	—	—
n-C_4	0.1	0.15	0.038	0	0	0	—
n-C_5	0.1	0.15	0.041	0	0	0	0
—	N_2	CO_2	C_1	C_2	C_3	n-C_4	n-C_5

for N_2 is calculated from $Q_{ex} = \int_0^{\infty} \rho(z)dz - \int_{\sigma_{sf}}^{\infty} \rho_b dz$, with ρ_b being the bulk density. **Fig. 2** shows good agreement between experiments and our calculations on the basis of ε_s/k_B=20 K, which is used in the rest of this work. Therefore, our theory does not contain adjustable parameters in the study of adsorption in a single carbon-slit nanopore and in porous media.

Results and Discussion

In the following, we first present the results of computations for adsorption and phase behavior in a single carbon-slit pore. Then, we verify the model predictions with measured adsorption data in activated carbons and dry coal for both pure substances and mixtures.

Adsorption and Desorption in a Single Carbon-Slit Nanopore. We first investigate the influence of type of species, temperature, and pore size on adsorption and desorption in a single carbon-slit pore. The absolute adsorption of component k per unit of inner PV is defined as $\rho_{ave,k} = \int_0^H \rho_k(z)dz/H_{in}$; that is, all molecules in the pore are included. $\rho_{ave,k}$ is also the average density of component k in the pore.

Fig. 3 depicts the adsorption and desorption isotherms of C_1, C_2, C_3, n-C_4, and n-C_5 at 303.15 K for H= 3 nm. Except for C_1 and to some extent C_2, all the other hydrocarbons show vapor/liquid transition in the bulk at the saturation pressure. For C_1 and C_2, because 303.15 K is higher than the critical temperature of C_1 and slightly lower than the critical temperature of C_2, no capillary condensation is observed. ρ_{ave} increases smoothly with pressure, and the adsorption and desorption processes completely overlap. For C_3, n-C_4, and n-C_5, because their critical temperatures are

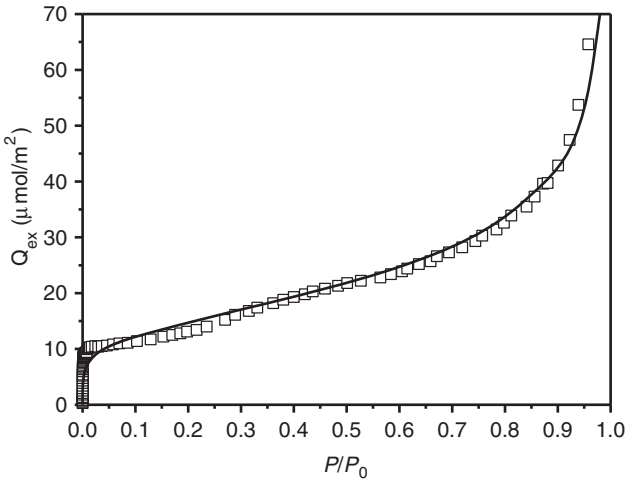

Fig. 2—Adsorption isotherm of N_2 on a Sterling graphite surface at 77.3 K. P_o is 1 atm, the saturation pressure of N_2 at 77.3 K. The symbols represent experiments by Ravikovitch et al. (2000) and Olivier (1995) and the line is from our calculation.

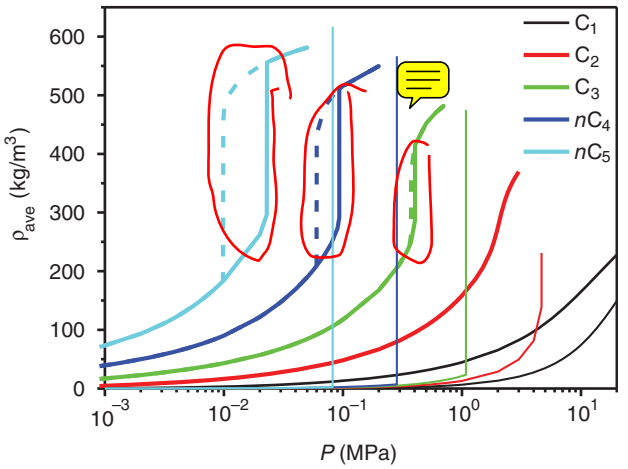

Fig. 3—Adsorption isotherms in a carbon-slit pore at 303.15 K and H= 3 nm for C_1, C_2, C_3, n-C_4, and n-C_5. Solid and dashed lines represent adsorption and desorption, respectively. The thin lines describe the bulk-density change with pressure.

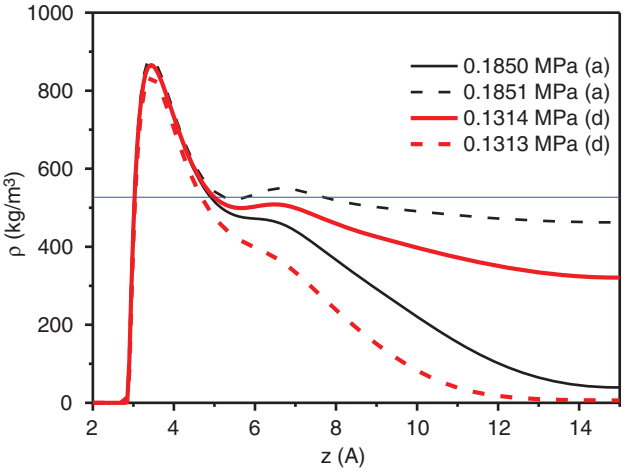

Fig. 4—Density distributions for C_3 in a carbon-slit pore at 273.15 K and $H = 3$ nm for 0.185 and 0.1851 MPa in adsorption and for 0.1314 and 0.1313 MPa in desorption. The thin line represents the equilibrium-liquid density.

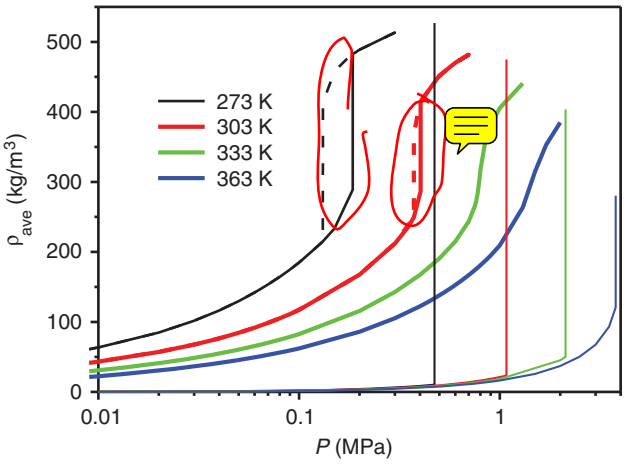

Fig. 5—Adsorption isotherms in a carbon-slit pore for C_3 and $H = 3$ nm at 273.15, 303.15, 333.15, and 363.15 K. Solid and dashed lines represent adsorption and desorption, respectively. The thin lines describe the bulk-density change with pressure.

much higher than 303.15 K, the adsorption isotherms entail a capillary condensation, and the difference in the adsorption and desorption processes gives rise to hysteresis. Both capillary condensation and vaporization (hysteresis) occur at a pressure lower than the saturation pressure, as the plots in Fig. 3 show. For capillary condensation, the behavior is similar to the Kelvin effect with lowering of the vapor pressure. As expected, the hysteresis becomes more pronounced as molar weight increases. The hysteresis is interpreted from thermodynamic metastability corresponding to a local minimum of free energy. The hysteresis in porous media is not as sharp as that in a single pore because porous media consist of many pores of different sizes that show hysteresis at different pressures. The hysteresis, or more generally adsorption amount in pores and in porous medium, are connected by the PSD.

The metastable phase transitions are recognized from the variation of density distribution with pressure, as illustrated in **Fig. 4** for C_3 at 273.15 K and $H = 3$ nm. We name the domain near the surface the adsorbed region and the domain near the pore center the free region. It should be emphasized that we only use these terms to help understand the phenomenon. In fact, when solving Eq. 3, we do not make any assumptions for the equilibrium-density distributions in the pore a priori. The computed-density distributions are smooth curves. Therefore, unlike traditional theories, our model could not distinguish between the adsorbed phase and free phase by artificially dividing a density profile into several regions. The adsorbed region may contain two adsorption layers. In the adsorption process, when the pressure slightly increases from 0.185 to 0.1851 MPa, the free region suddenly changes from vapor to condensed liquid, leading to a sudden increase in ρ_{ave}; that is, capillary condensation occurs. Conversely, in the desorption process, when the pressure slightly decreases from 0.1314 to 0.1313 MPa, the free region suddenly changes from condensed liquid to vapor, leading to a sudden decrease in ρ_{ave}; that is, capillary vaporization occurs. The density of the adsorbed region is not markedly affected, but the density of the free region changes significantly.

Fig. 5 shows the adsorption and desorption isotherms for C_3 at different temperatures for $H = 3$ nm. As expected, as the temperature increases, the hysteresis weakens, shifts toward higher pressures, and then vanishes, although the vapor/liquid transition occurs at all temperatures in the bulk. The effect of temperature is discussed further later.

Fig. 6 depicts the effect of pore size H on the adsorption and desorption behavior for C_1 and n-C_4 at 303.15 K. For C_1, ρ_{ave} increases continuously with pressure and there is no hysteresis because the critical temperature is much lower than 303.15 K. With increase of pore size, ρ_{ave} decreases because the share of the adsorbed region with much higher density decreases in relation to the free region with lower density. For n-C_4, the hysteresis appears and moves to higher pressure with increase in pore size.

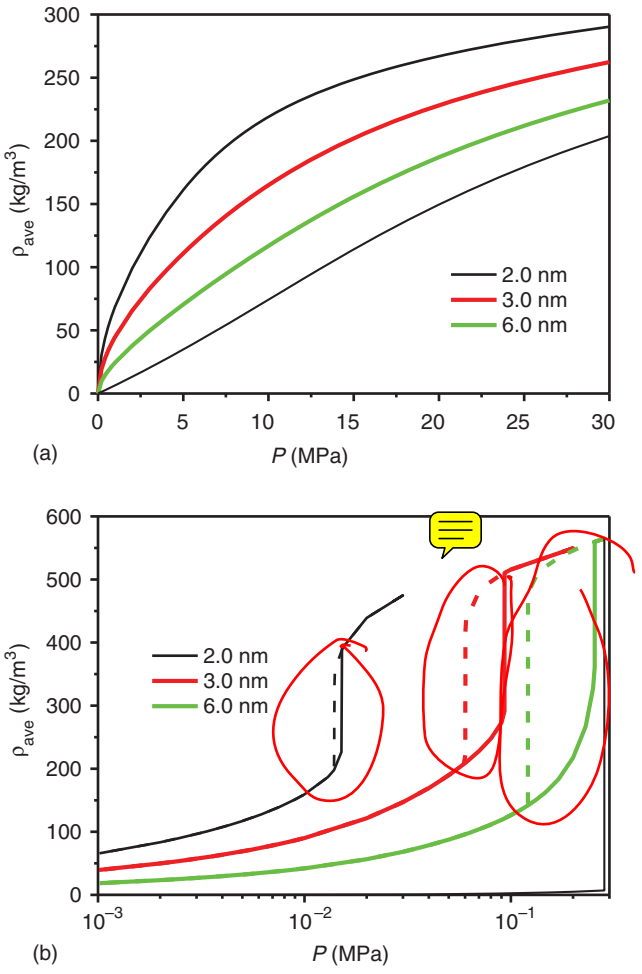

Fig. 6—Adsorption isotherms in a carbon-slit pore at 303.15 K for (a) C_1 and (b) n-C_4 at $H = 2$, 3, and 6 nm. Solid and dashed lines represent adsorption and desorption, respectively. The thin lines describe the bulk-density change with pressure.

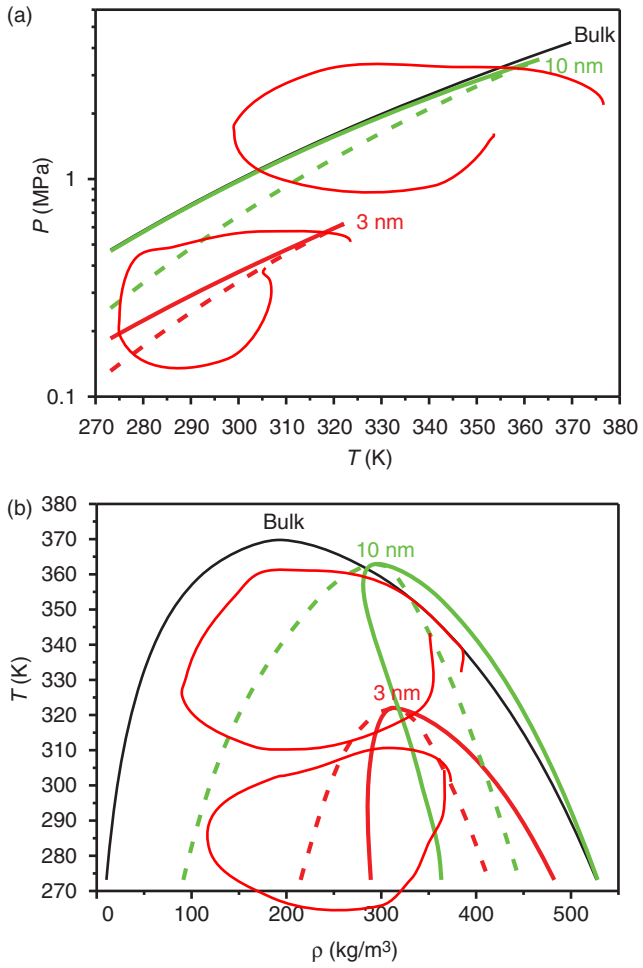

Fig. 7—Metastable phase transitions for C_3 in a carbon-slit pore with $H = 3$ and 10 nm in (a) P–T and (b) T–ρ diagrams. Solid and dashed lines represent adsorption and desorption, respectively. Bulk-equilibrium vapor and liquid densities and saturation pressures are also shown.

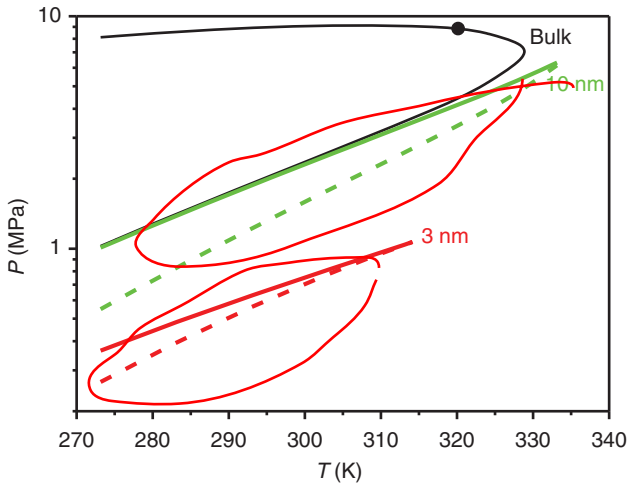

Fig. 8—Metastable phase transitions for the C_1/C_3 mixture (equal mole fractions in the bulk) in a carbon-slit pore with $H = 3$ and 10 nm in P–T diagram. Solid and dashed lines represent adsorption and desorption, respectively. Bulk-phase transition is also shown.

For $H = 6$ nm, the pressure at capillary condensation is close to the saturation pressure.

By use of the adsorption and desorption isotherms presented here, we construct the phase diagrams for the phase transitions in a carbon-slit pore. **Fig. 7** shows both the bulk and pore ($H = 3$ and 10 nm) phase diagrams in the P–T and T–ρ space for C_3. The PR-EOS with volume translation can faithfully reproduce the bulk-equilibrium vapor and liquid densities and saturation pressures even near the critical point (experimental data are not plotted). The metastable-phase transitions in the pore always take place at a pressure lower than the saturation pressure and at a temperature lower than the critical temperature. As the pore size increases, the fluid in the pore at capillary condensation becomes similar to that in the equilibrium bulk liquid. For the 3-nm pore, at capillary condensation, because the pressure is much lower than the saturation pressure, the free region has a density lower than the equilibrium bulk liquid (Fig. 4). Although the adsorbed region has significantly higher density than the equilibrium bulk liquid (Fig. 4), the average density in the pore is still lower than the equilibrium liquid density. For the 10-nm pore, at capillary condensation, because the pressure is close to the saturation pressure, the free region has a density close to the equilibrium bulk liquid. Because the adsorbed region has significantly higher density than the equilibrium bulk liquid, the average density in the pore is higher than the equilibrium liquid density.

Note that in Fig. 7a, the critical temperature and pressure change, as reported in the literature by others. However, these critical proprieties cannot be used in an EOS for the bulk phase with the expectation of correct P–T and T–ρ results in nanopores. The saturation pressures may be computed properly, but not the density results, which can be in error by a large factor.

The most important advantage of our DFT is that it is directly applicable to mixtures. **Fig. 8** presents the P–T phase diagram for the C_1/C_3 mixture (equal mole fractions in the bulk) in the pore ($H = 3$ and 10 nm) and in the bulk. There exists a retrograde region in the bulk when the temperature is higher than the critical temperature (solid circle). The same is shown in Fig. 7a, in which the phase transitions in the pore always take place at a pressure lower than the dewpoint pressure. Interestingly, above the cricondentherm where the bulk is always in single-phase state, the phase transitions still occur in the 10-nm pore but not in the 3-nm pore. The reason is that above the cricondentherm, the bulk-fluid molecules bear sufficient kinetic energy to overcome their potential energy. So the bulk is always in single-phase state because C_3 molecules cannot aggregate to form a liquid and lead to phase separation. In the pore, a higher-density C_3-rich adsorbed region still forms near each pore surface because the attraction between surface and C_3 molecules is stronger than the attraction between surface and C_1 molecules and attraction between C_3 molecules. As pressure increases, the adsorbed region becomes thicker and applies stronger attraction to the bulk-fluid molecules (especially C_3). In the 10-nm pore, there is always a free region near the pore center with properties close to the bulk. When the pressure (or adsorbed-region thickness) reaches an onset, capillary condensation occurs and bulk-fluid molecules (especially C_3) condense in the free region. In the 3-nm pore, before reaching its onset of condensation, the free region already disappears because of the connection of the two adsorbed regions.

To better understand the structural behavior of confined fluids, we present the compositional distributions of C_3 for the C_1/C_3 mixture (equal mole fractions in the bulk) in the pore ($H = 3$ and 10 nm) at 323.15 K and various pressures in **Fig. 9.** For a small pore ($H = 3$ nm), because the correlation between two walls are strong, C_1/C_3 mixtures do not reach the bulk limit in the middle of the pore; because of the strong surface attraction, the composition of C_3 in the middle is higher than that of C_1. The composition of C_3 in adsorption layer increases with pressure. However, it increases then decreases with pressure in the middle of the pores. When system temperature is higher than critical temperature but lower than cricondentherm temperature, both sides of the phase diagram is in gas phase. The composition of C_3 in the middle of the pore increases with pressure as it approaches lower dewpoint and decreases with pressure when it is higher than the upper dew pressure. Similar behavior can be seen for large pores ($H = 10$

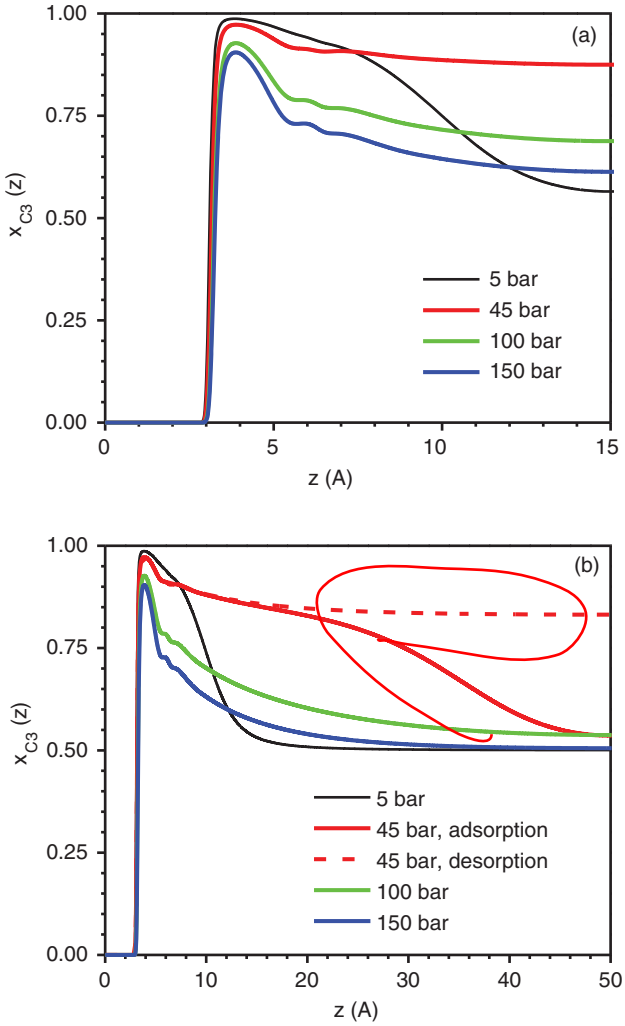

Fig. 9—Compositional distributions of C_3 for the C_1/C_3 mixture (equal mole fractions in the bulk) in a carbon-slit pore with (a) H = 3 nm and (b) H = 10 nm at 323.15 K and various pressures.

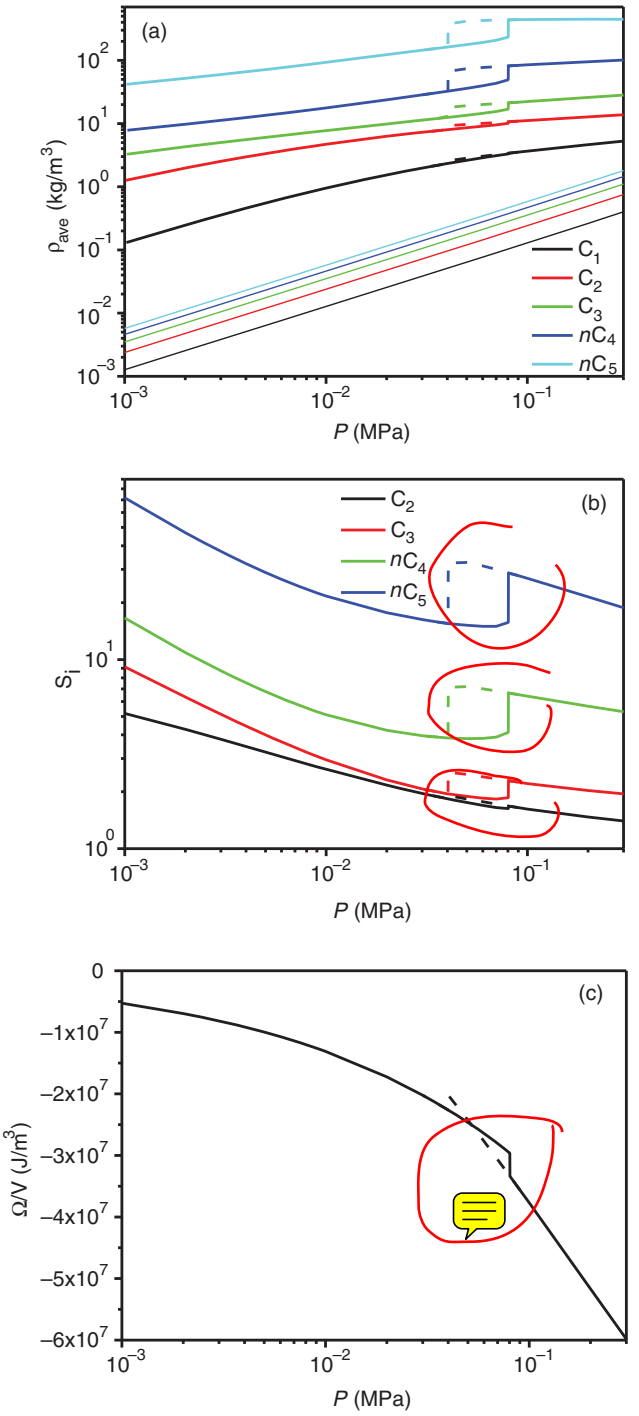

Fig. 10—(a) Adsorption isotherms, (b) selectivity curves to C_1, and (c) grand potential (per unit volume) vs. pressure in a carbon-slit pore at 303.15 K and H = 3 nm for the $C_1/C_2/C_3/n$-C_4/n-C_5 mixture (equal mole fractions in the bulk) when the pressure is lower than the bulk dewpoint pressure of 0.3103 MPa (the bulk is in single-vapor state). Solid and dashed lines represent adsorption and desorption, respectively. The thin lines describe the bulk-density change with pressure in Fig. 10a.

nm). Because the pore size is large enough, at low pressure (P = 5 bar) and high pressure (P = 150 bar) the composition of C_3 reaches the bulk limit in the middle of the pores. In addition, hysteresis of C_1/C_3 mixture is observed at 45 bar.

Fig. 10 presents our results for the adsorption of $C_1/C_2/C_3/n$-C_4/n-C_5 mixture (equal mole fractions in bulk) at 303.15 K for H = 3 nm when the pressure is lower than the bulk dewpoint pressure of 0.3103 MPa (the bulk is in single-vapor state). Figs. 10a and 10b present the adsorption isotherms and selectivity curves to C_1 for all the components. The selectivity of component k to C_1 is defined as $S_k = (x_k^p/x_{C_1}^p)/(x_k^b/x_{C_1}^b)$, where x_k^p and x_k^b represent the average mole fraction in the pore and mole fraction in the bulk for component k, respectively. All the plots in Fig. 10 show hysteresis. The adsorption, selectivity, and hysteresis become more pronounced as the molar weight of a hydrocarbon component increases. Fig. 10c highlights the metastability of phase transitions in the pore by calculating Ω in both adsorption and desorption processes. In the hysteresis, a given pressure corresponds to two different minima of Ω or two different sets of equilibrium-density distributions. Each metastable-phase transition is manifested by a distinctive drop of Ω. If fluids are in the bulk with a small disturbance, the system will move to the global minimum, but not in porous media. In porous media and nanopores, we could have a negative pressure (metastable) without concern for change in time (Firoozabadi 1999). **Fig. 11** presents the density difference and composition difference of each component in the pore (H = 3 nm) and in the bulk for the $C_1/C_2/C_3/n$-C_4/n-C_5 mixture (equal mole fractions in bulk) at 303.15 K and 30 MPa, which is higher than the bubblepoint pressure of 5.1794 MPa (the bulk is in single-liquid state). The fluid properties in the nanopore still could be very different from those in the bulk, although the packing effect becomes dominant at this high pressure. The component that has stronger attraction with the pore surfaces and/or smaller molecular size is more likely to enter the nanopore. That leads to the convex shape of both curves in Fig. 11 because n-C_5 has the strongest attraction with the pore surfaces and C_1 has the smallest molecular size.

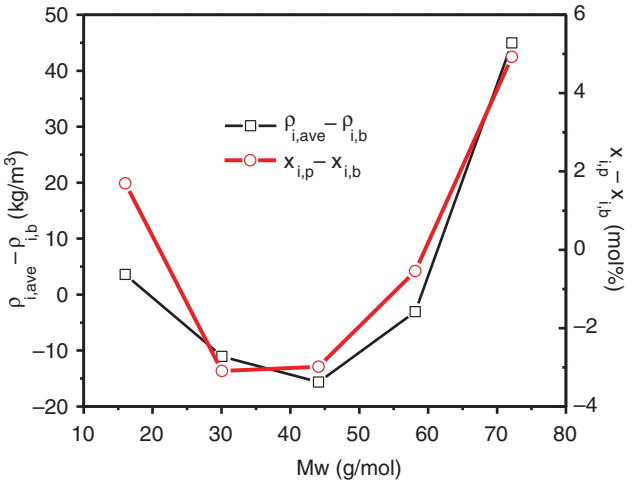

Fig. 11—Density difference and composition difference vs. species molar weight of each component in the pore and in the bulk for the $C_1/C_2/C_3/n\text{-}C_4/n\text{-}C_5$ mixture (equal mole fractions in the bulk) at 303.15 K and 30 MPa for H =3 nm, which is higher than the bubblepoint pressure of 5.1794 MPa (the bulk is in single-liquid state).

Pore-Structure Characterization and Adsorption Prediction in Activated Carbons. By use of a polydisperse carbon-slit pore model, we can characterize the pore structure and predict adsorption in activated carbons by the approximate solution of the adsorption integral:

$$\Gamma_k(T,P) = \int \rho_{\text{ave},k}(T,P,H_{\text{in}})PSD(H_{\text{in}})\text{d}H_{\text{in}}. \quad \ldots\ldots\ldots (5)$$

In Eq. 5, Γ_k is the experimental adsorption of component k in activated carbon. Three activated-carbon samples, AC-A (Qiao et al. 2000), AC-B (Dreibach et al. 1999), and AC-C (Sudibandriyo et al. 2003), are selected to examine our DFT model for both pore-structure characterization and adsorption prediction. We follow the same procedure for all the three samples. We first characterize the pore structure of activated carbon (i.e., solve for the PSD by minimizing the difference between measured and computed Γ of pure substances, and calculate the PV from $\int PSD(H_{\text{in}})\text{d}H_{\text{in}}$ and surface area (SA) from $2\int (PSD(H_{\text{in}})/H_{\text{in}})\text{d}H_{\text{in}})$. We then use the computed PSD to predict the adsorption of mixtures in the same activated carbon. We assume that the PSD follows the log-normal distribution $PSD(H_{\text{in}}) = \sum_{i=1}^{n} \frac{\alpha_i}{\sqrt{2\pi}\beta_i} \exp\left\{-\frac{[\ln(H_{\text{in}}) - \gamma_i]^2}{2\beta_i^2}\right\}$, with $3n$ unknown parameters α_i, β_i, and γ_i to be determined from the adsorption data of pure substances (Sweatman and Quirke 2001). The log-normal distribution is adopted for simplicity. The number of unknown parameters is determined by the best fit with experimental data. For the activated carbons, $n = 1$ (single-modal PSD) is already sufficient to reproduce the experiments. The calculated PSD is very narrow, approximately 1 nm for all three activated carbons.

Sample AC-A provides adsorption of C_1, C_2, C_3, and their binary mixtures at three temperatures: 303, 333, and 363 K to a pressure of 110 kPa (Qiao et al. 2000). We use all nine adsorption isotherms of the three pure substances at the three temperatures to obtain the PSD. The comparison between experiments and our calculations is shown in **Fig. 12a.** The agreement is good. As expected, the adsorption increases with the molar weight of hydrocarbon species and decreases with the temperature. Note that C_3 also shows the Langmuir-type adsorption isotherms because the pressures are much lower than the saturation pressure. The computed PSD is presented in Fig. 12b. From the PSD we estimate PV = 0.375 cm^3/g and SA = 876 m^2/g. The computed PSD, PV, and SA are close to the values reported by Qiao et al. (2000). The experiments on adsorption of three binary mixtures of C_1/C_2, C_1/C_3, and C_2/C_3 are available at a pressure of 50.6 kPa.

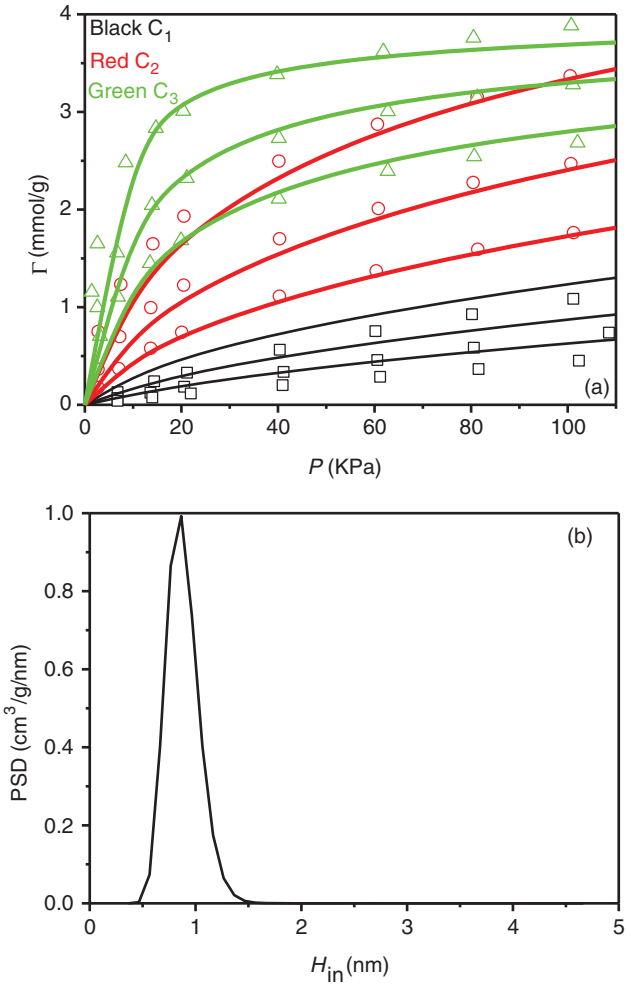

Fig. 12—(a) Adsorption isotherms for C_1, C_2, and C_3 in Sample AC-A. The symbols are experiments from Qiao et al. (2000), and lines are our calculations. For each group, the temperature is 303, 333, and 363 K (from top to bottom). (b) PSD of Sample AC-A.

The composition in the bulk is varied over the whole range. We predict the adsorption of these mixtures on the basis of known bulk composition at constant temperature and pressure. The measurements and our predictions are compared in **Fig. 13.** There is agreement over the whole bulk-composition range.

Sample AC-B covers the adsorption data of C_1, N_2, CO_2, and their binary and ternary mixtures at 298 K to 6 MPa (Dreibach et al. 1999). We determine the PSD by use of all three adsorption isotherms of the pure substances. **Fig. 14a** shows good agreement between measurements and our calculations. Fig. 14b presents the computed PSD. We estimate PV= 0.499 cm^3/g and SA= 858 m^2/g. By use of the computed PSD, the adsorption isotherms of mixtures are predicted. **Fig. 15** is for the binary mixtures of CO_2/N_2, C_1/N_2, and C_1/CO_2, and **Fig. 16** is for the ternary mixture $C_1/CO_2/N_2$. For each mixture, the bulk composition is fixed. In each figure, the adsorption isotherms are presented for both individual components and the total. Our predictions successfully capture the experiments.

The last example of activated carbon is on adsorption of C_1, N_2, CO_2, and their binary mixtures in Sample AC-C at 318.2 K to 14 MPa (Sudibandriyo et al. 2003). We compute the PSD on the basis of all three adsorption isotherms of pure substances. As shown in **Fig. 17a,** the agreement is good, except the adsorption of N_2 is somewhat overestimated at high pressures. From the PSD shown in Fig. 17b, we estimate PV= 0.39 cm^3/g and SA= 613 m^2/g. Sample AC-C has lower PV and SA than Sample AC-B. With the computed PSD, we predict the adsorption isotherms of the binary mixtures of CO_2/N_2, N_2/C_1, and CO_2/C_1 at the fixed bulk composition. **Fig. 18** presents the comparison between measurements and our predictions for the adsorption isotherms. In mixtures CO_2/N_2 and

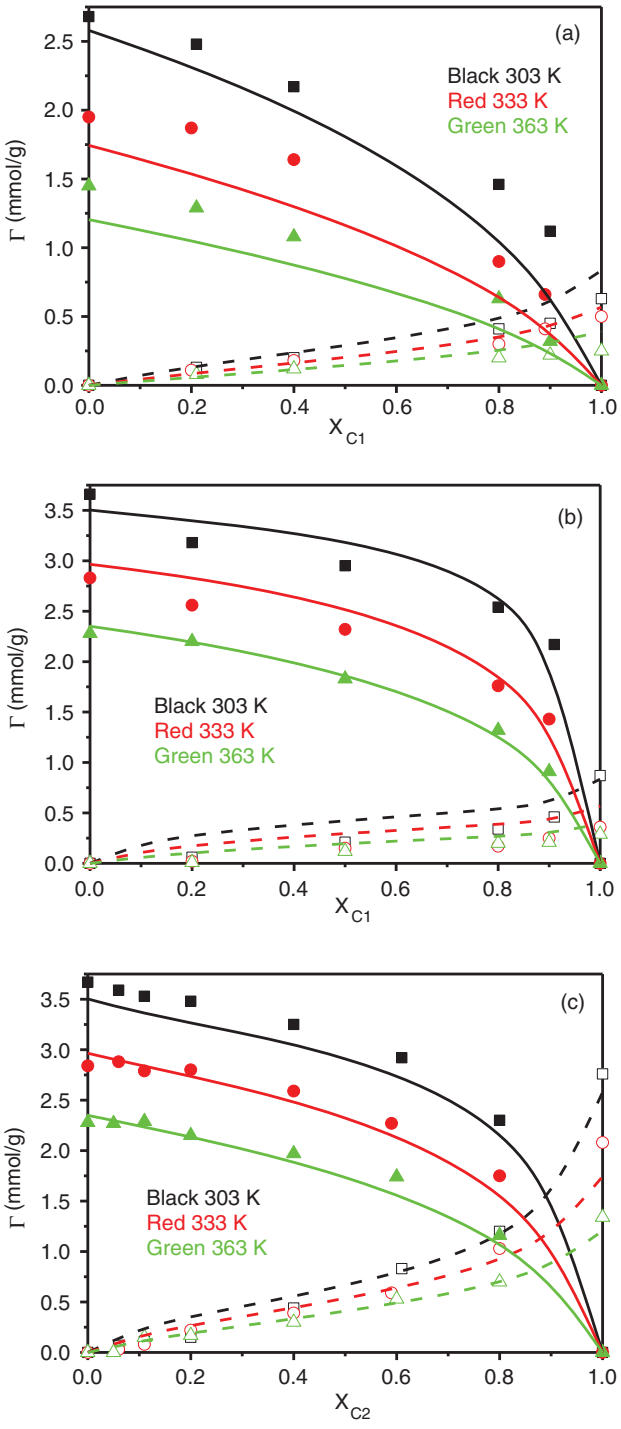

Fig. 13—Adsorption for mixtures (a) C_1/C_2, (b) C_1/C_3, and (c) C_2/C_3 as function of mole fraction of lighter component in the bulk at 50.6 kPa in Sample AC-A. The symbols are experiments from Qiao et al. (2000), and lines are our predictions. The filled symbols and solid lines are for the heavier component. The empty symbols and dashed lines are for the lighter component.

N_2/C_1, the adsorption isotherms of components are captured when the pressure is not too high. The agreement deteriorates when the pressure exceeds 7 MPa, especially for N_2. However, the adsorption isotherms of the total are faithfully reproduced in the whole pressure range. For the mixture CO_2/C_1, the agreement is excellent for all three adsorption isotherms.

Pore-Structure Characterization and Adsorption Prediction in Dry Coal. Similar to the gas adsorption in activated carbons, we model adsorption in Sulcis dry coal by assuming its pore structure to be described by the polydisperse carbon-slit pore (Ottiger et al. 2008a,2008b) In this case, the excess adsorption isotherms of pure substances and their mixtures are available. The excess adsorption of component k per unit of inner PV is defined as $\rho_{\text{ave},k,\text{ex}} = \int_0^H [\rho_k(z) - \rho_{k,b}]\text{d}z/H_{\text{in}}$, where $\rho_{k,b}$ is the bulk density of component k. The adsorption integral (Eq. 5) is used to characterize the pore structure and predict the adsorption in the dry coal, except the Γ_k and $\rho_{\text{ave},k}$ are replaced by the $\Gamma_{k,\text{ex}}$ and $\rho_{\text{ave},k,\text{ex}}$, respectively. As the pressure increases, the excess adsorption may increase at relatively low pressures because of strong surface attraction and enough empty pore space, but decrease at high pressures because the pore is nearly saturated. This is in contrast to the absolute adsorption that always increases with pressure but with decreasing slope (Fig. 6a).

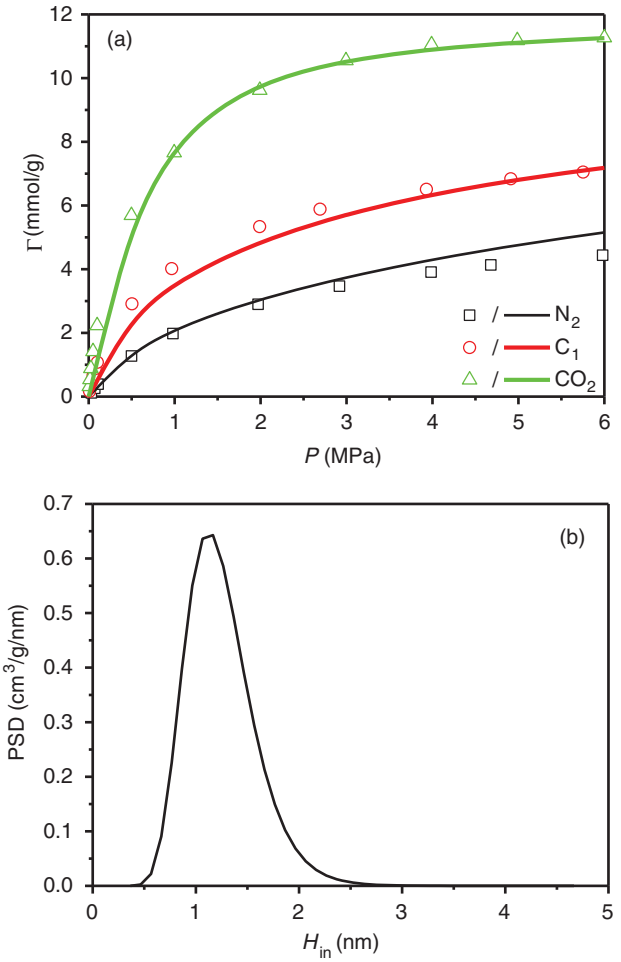

Fig. 14—(a) Adsorption isotherms for N_2, C_1, and CO_2 in Sample AC-B at 298 K. The symbols are experiments from Dreibach et al. (1999), and lines are our calculations. (b) PSD of Sample AC-B.

We first use the adsorption isotherms of C_1 and CO_2 in the dry coal at 318.15 K to 18 MPa to obtain the PSD, and then predict the adsorption isotherms of their binary mixtures with varying bulk compositions. Both experiments and our calculations are presented in **Fig. 19a.** To facilitate the comparison, only the adsorption isotherms of CO_2 are shown for the mixture adsorptions. The overall agreement is good. All the adsorption isotherms demonstrate the nonmonotonic behavior with pressure. The nonmonotonicity becomes stronger with the increase of CO_2 concentration in the bulk. That is because the attraction between pore and CO_2 is much stronger than that between pore and C_1. As a result, the pore becomes readily saturated by CO_2 with the bulk at higher CO_2 concentration. Our DFT faithfully captures this trend. The correlated PSD is presented in Fig. 19b. For this coal, $n = 2$ (bimodal PSD) can provide satisfactory fits to the experiments. The PSD is much wider than that for the activated carbons, but the

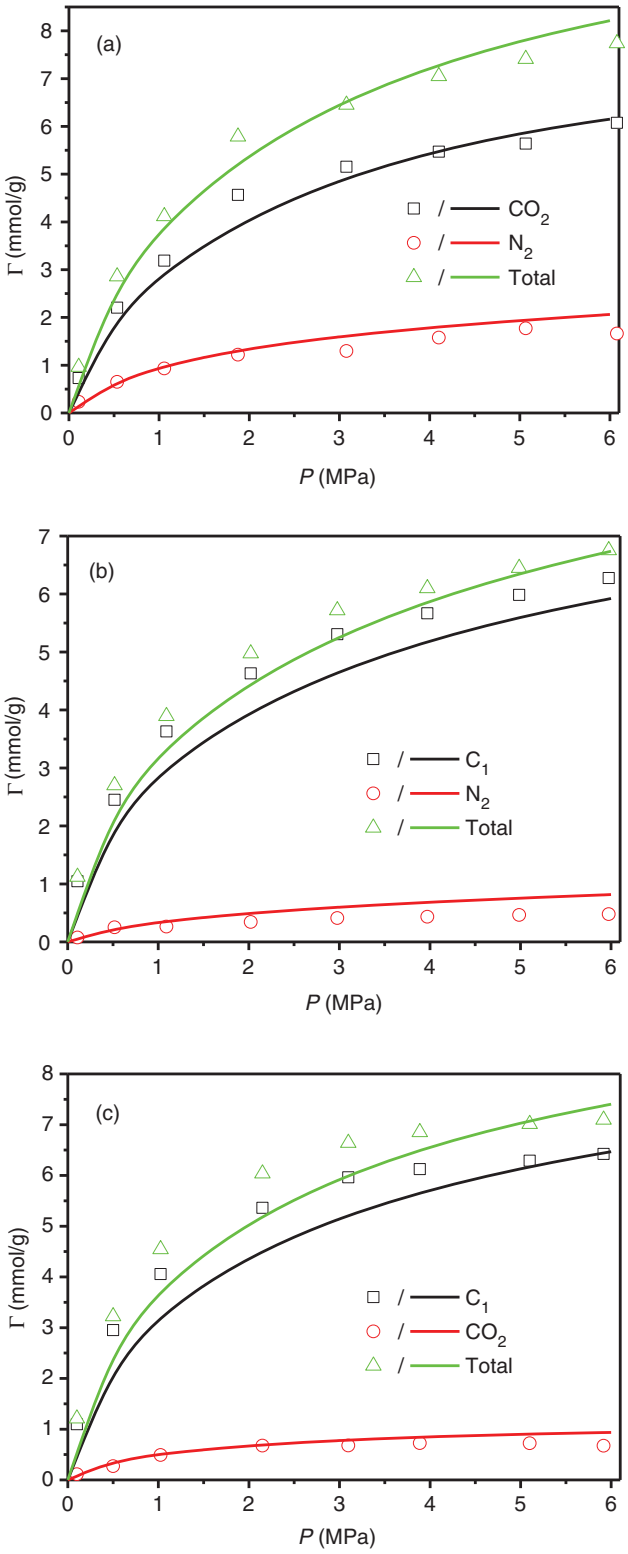

Fig. 15—Adsorption isotherms for individual components and the total for mixtures (a) CO_2/N_2 (mol/mol = 0.2/0.8 in the bulk), (b) C_1/N_2 (mol/mol = 0.72/0.28 in the bulk), and (c) C_1/CO_2 (mol/mol = 0.95/0.05 in the bulk) in Sample AC-B at 298 K. The symbols are experiments from Dreibach et al. (1999), and lines are our predictions.

majority of the pores are at approximately 1 nm. On the basis of the PSD, we estimate PV= 0.19 cm^3/g and SA= 235 m^2/g for this dry coal. The reported PV= 0.2 cm^3/g is in good agreement with our prediction. In addition, the pores in the PSD obtained by Ottiger et al. (2008b) are mainly in the region of <2 nm, in line with our calculations.

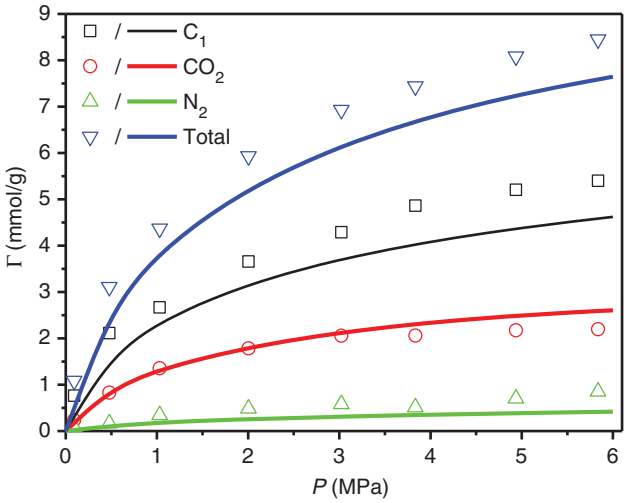

Fig. 16—Adsorption isotherms for individual components and the total for the mixture $C_1/CO_2/N_2$ (mol/mol/mol = 0.72/0.12/0.16 in the bulk) in Sample AC-B at 298 K. The symbols are experiments from Dreibach et al. (1999), and lines are our predictions.

Conclusions

The long-term objective of our work relates to the modeling of adsorption/desorption and phase behavior of hydrocarbons, CO_2, N_2, water, and their mixtures in shale. Our examination of shale

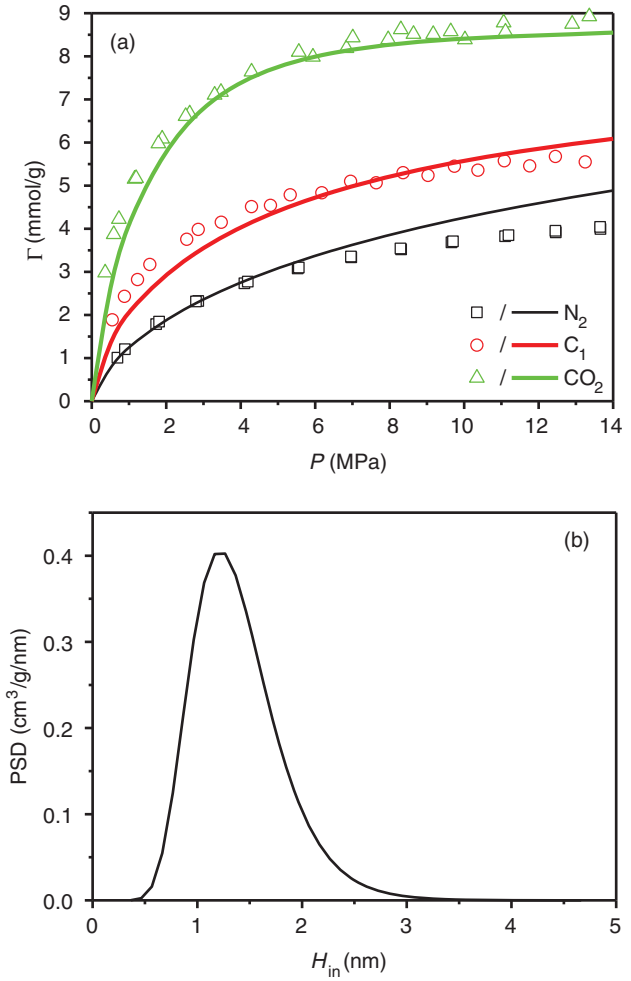

Fig. 17—(a) Adsorption isotherms for N_2, C_1, and CO_2 in Sample AC-C at 318.2 K. The symbols are experiments from Sudibandriyo et al. (2003), and lines are our calculations. (b) PSD of Sample AC-C.

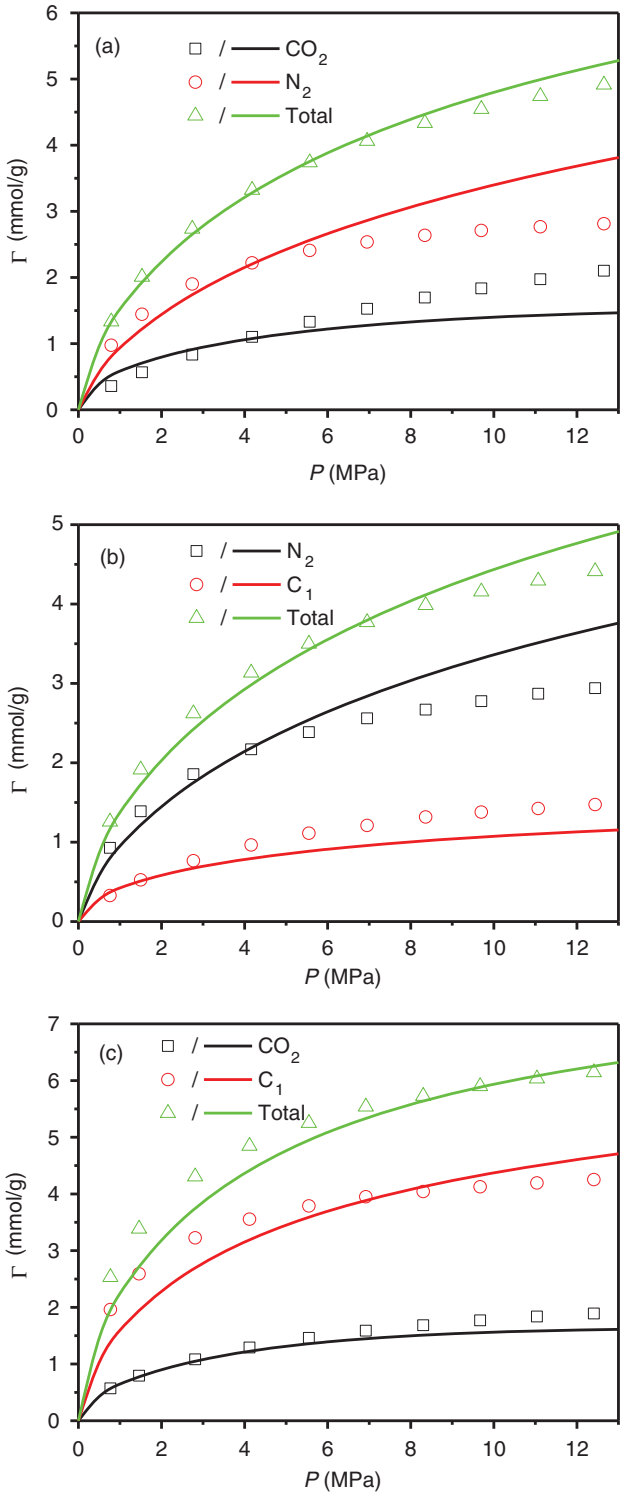

Fig. 18—Adsorption isotherms for individual components and the total for mixtures (a) CO_2/N_2 (mol/mol = 0.06/0.94 in the bulk), (b) C_1/N_2 (mol/mol = 0.12/0.88 in the bulk), and (c) C_1/CO_2 (mol/mol = 0.87/0.13 in the bulk) in Sample AC-C at 318.2 K. The symbols are experiments from Sudibandriyo et al. (2003), and lines are our predictions.

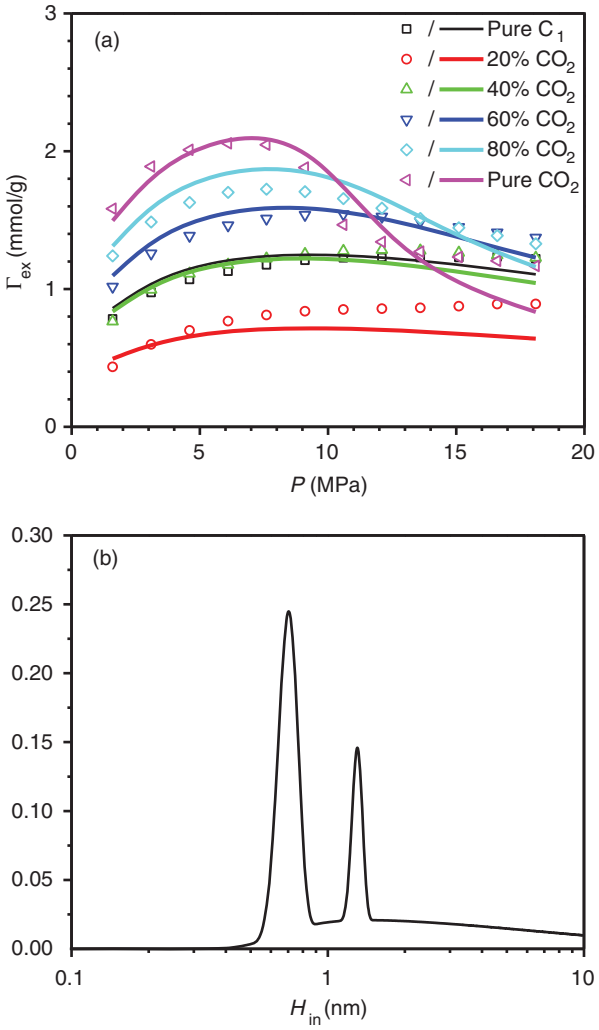

Fig. 19—(a) Adsorption isotherms of pure C_1 and CO_2, and CO_2 in C_1/CO_2 mixtures (different CO_2 concentrations in terms of mol% in the bulk) in dry coal at 318.15 K. The symbols are experiments from Ottiger et al. (2008a,2008b), and lines are our calculations. (b) PSD of the dry coal.

data reveals that the shale chemistry plays a significant role in phase behavior and adsorption. Different surface chemistries in shale have different interaction energies with fluid molecules. This work is the first step in that direction.

In this paper, we present a systematic investigation of adsorption and phase behavior of pure hydrocarbons, CO_2, N_2, and their mixtures in carbon nanopores and in activated carbon and dry coal composed of carbon nanopores. The DFT combined with the PR-EOS is applied in the modeling and computation. Our DFT possesses significant advantages over traditional methods, especially in the explicit representation of fluid/fluid and fluid/surface interactions. The former is described by the "heterogeneous" PR-EOS, and the latter is represented by the Steele 10-4-3 potential. The main conclusions drawn from this work are:

- For pure hydrocarbons in nanopores, capillary condensation and hysteresis are more likely in heavier species, at lower temperatures, and in smaller pores. Phase change takes place below the saturation pressure and critical temperature. The average density at capillary condensation could be either higher (in larger pores) or lower (in smaller pores) than that of equilibrium bulk liquid. Some of these finding are consistent with results from Monte Carlo simulations (Jiang and Sandler 2005; Singh et al. 2009).
- The phase behavior of mixtures becomes more complicated in nanopores. Above the cricondentherm, capillary condensation and hysteresis may still occur in nanopores although the bulk stays in single-phase state. This behavior has not been reported in the past.
- In activated carbons and dry coal, we reproduce the adsorption isotherms of various pure substances with a unique PSD. In the past work using DFT and GCMC, different PSDs of the same medium have to be adopted to capture the adsorption of different species. By use of the unique PSD, we predict the adsorption of mixtures at various conditions in the same porous material.

- Our theory provides a unified framework for both monolayer and multilayer adsorptions, for both pure substances and mixtures, in both single nanopores and porous media, and for both pore-structure characterization and adsorption estimation. For larger hydrocarbon molecules, orientation effects should be accounted for also, and this aspect is currently under consideration.

Nomenclature

$F\{[\rho_k(\mathbf{r})]\}$ = Helmholtz energy functional
$F^{ex}\{[\rho_k(\mathbf{r})]\}$ = excess Helmholtz energy functional
$F^{id}\{[\rho_k(\mathbf{r})]\}$ = ideal Helmholtz energy functional
H = apparent size of slit pore
H_{in} = effective pore size
k_B = Boltzmann constant
M_w = molar weight
P_c = critical pressure
PSD = pore-size distribution
Q_{ex} = excess adsorption per unit surface area
S_k = selectivity of component k
T = absolute temperature
T_c = critical temperature
$U_{sk}(z)$ = surface attraction on component k at position z
x_k^p = average mole fraction of component k in the pore
x_k^b = average mole fraction of component k in the bulk
Γ_k = absolute adsorption of component k in porous media
$\Gamma_{k,\text{ex}}$ = excess adsorption of component k in porous media
Δ = interlayer spacing of graphite
ε_k = attraction-energy parameter of component k
ε_s = attraction-energy parameter of surface molecules
ε_{sk} = energy parameter of fluid-wall interaction
μ_k = chemical potential of component k
$\rho_{\text{ave},k}$ = absolute adsorption of component k per unit of inner pore volume
$\rho_{\text{ave},k,\text{ex}}$ = excess adsorption of component k per unit of inner pore volume
$\rho_{k,b}$ = bulk density of component k
$\rho_k(\mathbf{r})$ = density distribution of component k at position $\mathbf{r}$
ρ_s = density of graphite
σ_k = "molecular diameter" of component k
σ_{sk} = size parameter of fluid-wall interaction
$\Psi_k(\mathbf{r})$ = external potential of component k at position r
ω = acentric factor
$\Omega\{[\rho_k(\mathbf{r})]\}$ = grand potential functional

Acknowledgments

This research was sponsored by the member companies of the Reservoir Engineering Research Institute (RERI), Palo Alto, California. Their support is greatly appreciated.

References

Adesida, A.G., Akkutlu, I.Y., Resasco, D.E., et al. 2011. Characterization of Barnett Shale Kerogen Pore Size Distribution using DFT Analysis and Grand Canonical Monte Carlo Simulations. Presented at SPE Annual Technical Conference and Exhibition, Denver, Colorado, 30 October–2 November. SPE-147397-MS. http://dx.doi.org/10.2118/147397-MS.

Barret, E.P., Joyner, L.G., and Halenda, P.H. 1951. The Determination of Pore Volume and Area Distributions in Porous Substances. I. Computations from Nitrogen Isotherms. *J. Am. Chem. Soc.* **73** (1): 373–380. http://dx.doi.org/10.1021/ja01145a126.

Brunauer, S., Emmett, P.H., and Teller, E. 1938. Adsorption of Gases in Multimolecular Layers. *J. Am. Chem. Soc.* **60** (2): 309–319. http://dx.doi.org/10.1021/ja01269a023.

Chapman, W.G., Gubbins, K.E., Jackson, G., et al. 1989. SAFT: Equation-of-State Solution Model for Associating Fluids. *Fluid Phase Equilibr.* **52** (December): 31–38. http://dx.doi.org/10.1016/0378-3812(89)80308-5.

Chapman, W.G., Gubbins, K.E., Jackson, G., et al. 1990. New Reference Equation of State for Associating Liquids. *Ind. Eng. Chem. Res.* **29** (8): 1709–1721. http://dx.doi.org/10.1021/ie00104a021.

Chapman, W.G., Jackson, G., and Gubbins, K.E. 1988. Phase Equilibria of Associating Fluids. Chain Molecules with Multiple Bonding Sites. *Mol. Phys.* **65** (5): 1057–1079. http://dx.doi.org/10.1080/00268978800101601.

Cohan, L.H. 1938. Sorption Hysteresis and the Vapor Pressure of Concave Surfaces. *J. Am. Chem. Soc.* **60** (2): 433–435. http://dx.doi.org/10.1021/ja01269a058.

Dreibach, F., Staudt, R., and Keller, J.U. 1999. High Pressure Adsorption Data of Methane, Nitrogen, Carbon Dioxide and their Binary and Ternary Mixtures on Activated Carbon. *Adsorption* **5** (3): 215–227. http://dx.doi.org/10.1023/A:1008914703884.

Ebner, C. and Saam, W.F. 1977. New Phase-Transition Phenomena in Thin Argon Films. *Phys. Rev. Lett.* **38** (25): 1486–1489. http://dx.doi.org/10.1103/PhysRevLett.38.1486.

Ebner, C., Saam, W.F., and Stroud, D. 1976. Density-Functional Theory of Simple Classical Fluids. I. Surfaces. *Phys. Rev. A* **14** (6): 2264–2273. http://dx.doi.org/10.1103/PhysRevA.14.2264.

Evans, R. 1996. Density Functionals in the Theory of Nonuniform Fuids. In *Fundamentals of Inhomogeneous Fluids*, ed. D. Henderson, Chap. 3, 85–176. New York City, New York: Marcel Dekker.

Firoozabadi, A. 1999. *Thermodynamics of Hydrocarbon Reservoirs*. New York City, New York: McGraw-Hill.

Gelb, L.D., Gubbins, K.E., Radhakrishnan, R., et al. 1999. Phase Separation in Confined Systems. *Rep. Prog. Phys.* **62** (12): 1573–1659. http://dx.doi.org/10.1088/0034-4885/62/12/201.

Halsey, G.D. 1948. Physical Adsorption on Non-Uniform Surfaces. *J. Chem. Phys.* **16:** 931–937. http://dx.doi.org/10.1063/1.1746689.

Jhaveri, B.S. and Youngren, G.K. 1988. Three-Parameter Modification of the Peng-Robinson Equation of State To Improve Volumetric Predictions. *SPE Res Eval & Eng* **3** (3): 1033–1040. SPE-13118-PA. http://dx.doi.org/10.2118/13118-PA.

Jiang, J.W. and Sandler, S.I. 2005. Adsorption and Phase Transitions on Nanoporous Carbonaceous Materials: Insights from Molecular Simulations. *Fluid Phase Equilibria.* **228–229:** 189–195. http://dx.doi.org/10.1016/j.fluid.2004.08.014.

Kuila, U. and Prasad, M. 2011. Understanding Pore-Structure And Permeability In Shales. Presented at SPE Annual Technical Conference and Exhibition, Denver, Colorado, 30 October–2 November. SPE-146869-MS. http://dx.doi.org/10.2118/146869-MS.

Langmuir, I. 1916. The Constitution and Fundamental Properties of Solids and Liquids. Part I. Solids. *J. Am. Chem. Soc.* **38** (11): 2221–2295. http://dx.doi.org/10.1021/ja02268a002.

Li, Z. and Firoozabadi, A. 2009. Interfacial Tension of Nonassociating Pure Substances and Binary Mixtures by Density Functional Theory Combined with Peng–Robinson Equation of State. *J. Chem. Phys.* **130** (15): 154108. http://dx.doi.org/10.1063/1.3100237.

Montgomery, S.L., Javie, D.M., Bowker, K.A., et al. 2005. Mississippian Barnett Shale, Fort Worth Basin, North-Central Texas: Gas-Shale Play with Multi–Trillion Cubic Foot Potential. *AAPG Bull.* **89** (2): 155–175. http://dx.doi.org/10.1306/09170404042.

Monsalvo, M. and Shapiro, A. 2007. Modeling Adsorption of Binary and Ternary Mixtures on Microporous Media. *Fluid Phase Equilibr.* **254** (1–2): 91–100. http://dx.doi.org/10.1016/j.fluid.2007.02.006.

Monsalvo, M. and Shapiro, A. 2009a. Modeling Adsorption of Liquid Mixtures on Porous Materials. *J. Colloid Interf. Sci.* **333** (1): 310–316. http://dx.doi.org/10.1016/j.jcis.2009.01.055.

Monsalvo, M. and Shapiro, A. 2009b. Study of High-Pressure Adsorption from Supercritical Fluids by the Potential Theory. *Fluid Phase Equilibr.* **283** (1–2): 56–64. http://dx.doi.org/10.1016/j.fluid.2009.05.015.

Myers, A.L. and Prausnitz, J.M. 1965. Thermodynamics of Mixed-Gas Adsorption. *AIChE J.* **11** (1): 121–127. http://dx.doi.org/10.1002/aic.690110125.

Olivier, J.P. 1995. Modeling Physical Adsorption on Porous and Nonporous Solids Using Density Functional Theory. *J. Porous Mat.* **2** (1): 9–17. http://dx.doi.org/10.1007/BF00486565.

Ottiger, S., Pini, R., Storti, G., et al. 2008a. Competitive Adsorption Equilibria of CO_2 and CH_4 on a Dry Coal. *Adsorption* **14** (4–5): 539–556. http://dx.doi.org/10.1007/s10450-008-9114-0.

Ottiger, S., Pini, R., Storti, G., et al. 2008b. Measuring and Modeling the Competitive Adsorption of CO_2, CH_4, and N_2 on a Dry Coal. *Langmuir* **24** (17): 9531–9540. http://dx.doi.org/10.1021/la801350h.

Peng, D.Y. and Robinson, D.B. 1976. A New Two-Constant Equation of State. *Ind. Eng. Chem. Fundamen.* **15** (1): 59–64. http://dx.doi.org/10.1021/i160057a011.

Qiao, S.Z., Wang, K., and Hu, X.J. 2000. Using Local IAST with Micropore Size Distribution To Predict Multicomponent Adsorption Equilibrium of Gases in Activated Carbon. *Langmuir* **16** (3): 1292–1298. http://dx.doi.org/10.1021/la990785q.

Rangarajan, B., Lira, C.T., and Subramanian, R. 1995. Simplified Local Density Model for Adsorption Over Large Pressure Ranges. *AIChE J.* **41** (4): 838–845. http://dx.doi.org/10.1002/aic.690410411.

Ravikovitch, P.I., Vishnyakov, A., Russo, R., et al. 2000. Unified Approach to Pore Size Characterization of Microporous Carbonaceous Materials from N_2, Ar, and CO_2 Adsorption Isotherms. *Langmuir* **16** (5): 2311–2320. http://dx.doi.org/10.1021/la991011c.

Robinson, D.B., Peng, D.Y., and Chung, S.Y.K. 1985. The Development of the Peng-Robinson Equation and its Application to Phase Equilibrium in a System Containing Methanol. *Fluid Phase Equilibr.* **24** (1–2): 25–41. http://dx.doi.org/10.1016/0378-3812(85)87035-7.

Roque-Malherbe, R.M.A. 2007. *Adsorption and Diffusion in Nanoporous Materials*. Boca Raton, Florida: CRC Press.

Rosenfeld, Y. 1989. Free-Energy Model for the Inhomogeneous Hard-Sphere Fluid Mixture and Density-Functional Theory of Freezing. *Phys. Rev. Lett.* **63** (9): 980–983. http://dx.doi.org/10.1103/PhysRevLett.63.980.

Shapiro, A. and Stenby, E. 1998. Analysis of Multicomponent Adsorption Close to a Dew Point. *J. Colloid Interf. Sci.* **206** (2): 546–557. http://dx.doi.org/10.1006/jcis.1998.5683.

Singh, S.K., Sinha, A., Deo, G., et al. 2009. Vapor–Liquid Phase Coexistence, Critical Properties, and Surface Tension of Confined Alkanes. *J. Phys. Chem. C* **113** (17): 7170–7180. http://dx.doi.org/10.1021/jp8073915.

Steele, W.A. 1973. The Physical Interaction of Gases with Crystalline Solids: I. Gas-Solid Energies and Properties of Isolated Adsorbed Atoms. *Surf. Sci.* **36** (1): 317–352. http://dx.doi.org/10.1016/0039-6028(73)90264-1.

Subramanian, R., Pyada, H., and Lira, C.T. 1995. An Engineering Model for Adsorption of Gases onto Flat Surfaces and Clustering in Supercritical Fluids. *Ind. Eng. Chem. Res.* **34** (11): 3830–3837. http://dx.doi.org/10.1021/ie00038a021.

Sudibandriyo, M., Pan, Z.J., Fitzgerald, J.E., et al. 2003. Adsorption of Methane, Nitrogen, Carbon Dioxide, and Their Binary Mixtures on Dry Activated Carbon at 318.2 K and Pressures up to 13.6 Mpa. *Langmuir* **19** (13): 5323–5331. http://dx.doi.org/10.1021/la020976k.

Sweatman, M.B. and Quirke, N. 2001. Characterization of Porous Materials by Gas Adsorption at Ambient Temperatures and High Pressure. *J. Phys. Chem. B* **105** (7): 1403–1411. http://dx.doi.org/10.1021/jp003308l.

Sweatman, M.B. and Quirke, N. 2002. Predicting the Adsorption of Gas Mixtures: Adsorbed Solution Theory versus Classical Density Functional Theory. *Langmuir* **18** (26): 10443–10454. http://dx.doi.org/10.1021/la0200358.

Ustinov, E.A., and Do, D.D. 2003. High-Pressure Adsorption of Supercritical Gases on Activated Carbons: An Improved Approach Based on the Density Functional Theory and the Bender Equation of State. *Langmuir* **19** (20): 8349–8357. http://dx.doi.org/10.1021/la030119w.

Wu, J. 2006. Density Functional Theory for Chemical Engineering: From Capillarity to Soft Materials. *AIChE J.* **52** (3): 1169–1193. http://dx.doi.org/10.1002/aic.10713.

Wu, J. 2009. Density Functional Theory for Liquid Structure and Thermodynamics. In *Molecular Thermodynamics of Complex Systems*, ed. X.H. Lu and Y. Hu, Chap. 1, 1–73. Berlin, Germany: Structure and Bonding Series, Vol. 131, Springer.

Wu, J. and Li, Z. 2007. Density-Functional Theory for Complex Fluids. *Annu. Rev. Phys. Chem.* **58:** 85–112. http://dx.doi.org/10.1146/annurev.physchem.58.032806.104650.

Appendix A—Classical DFT

DFT constructs an analytical connection between thermodynamic functions and average or equilibrium distribution of particles $\rho(\mathbf{r})$. Considering a system containing N identical particles, $\rho(\mathbf{r})$ is defined as the ensemble average of instantaneous density profile $\hat{\rho}(\mathbf{r})$,

$$\rho(\mathbf{r}) = \langle \hat{\rho}(\mathbf{r}) \rangle = \left\langle \sum_{i=1}^{N} \delta(\mathbf{r}_i - \mathbf{r}) \right\rangle, \quad \text{. . . . . (A-1)}$$

where $\mathbf{r}_i$ is the position of particle i, δ is the Dirac delta function, and $\langle\rangle$ denotes the ensemble average. The total energy of the system E (Hamiltonian) includes three contributions: kinetic energy, intermolecular interaction Φ, and external potential Ψ,

$$E = \sum_{i=1}^{N} \frac{\mathbf{p}_i^2}{2m} + \Phi(\mathbf{r}^N) + \sum_{i=1}^{N} \Psi(\mathbf{r}_i), \quad \text{. . . . . (A-2)}$$

where $\mathbf{p}_i$ is the momentum of particle i, m is the mass of each particle, and $\mathbf{r}^N = (\mathbf{r}_1, \mathbf{r}_2, \ldots, \mathbf{r}_N)$ is the configuration. For an open system, the grand partition function Ξ is given by

$$\begin{aligned} \Xi &= \sum_N \frac{1}{N! h^{3N}} \int \mathrm{d}\mathbf{r}^N \mathrm{d}\mathbf{p}^N \exp[-\beta(E - N\mu)] \\ &= \sum_N \frac{1}{N! \Lambda^{3N}} \int \mathrm{d}\mathbf{r}^N \exp\left\{ -\beta \left[\Phi(\mathbf{r}^N) + \sum_{i=1}^{N} \Psi(\mathbf{r}_i) - N\mu \right] \right\}, \end{aligned} \quad \text{. . . . . (A-3)}$$

where h is the Planck constant, μ is the chemical potential, $\Lambda = h/\sqrt{2\pi m k_B T}$ is the thermal wavelength, $\mathrm{d}\mathbf{r}^N = \mathrm{d}\mathbf{r}_1 \mathrm{d}\mathbf{r}_2 \ldots \mathrm{d}\mathbf{r}_N$, and $\mathrm{d}\mathbf{p}^N = \mathrm{d}\mathbf{p}_1 \mathrm{d}\mathbf{p}_2 \ldots \mathrm{d}\mathbf{p}_N$. $\rho(\mathbf{r})$ is related to E and Ξ through

$$\begin{aligned} \rho(\mathbf{r}) &= \frac{1}{\Xi} \sum_N \frac{1}{N! \Lambda^{3N}} \int \mathrm{d}\mathbf{r}_1 \mathrm{d}\mathbf{r}_2 \ldots \mathrm{d}\mathbf{r}_N \sum_{i=1}^{N} \delta(\mathbf{r}_i - \mathbf{r}) \\ &\quad \times \exp\left\{ -\beta \left[\Phi(\mathbf{r}_1, \mathbf{r}_2, \ldots, \mathbf{r}_N) + \sum_{i=1}^{N} \Psi(\mathbf{r}_i) - N\mu \right] \right\} \\ &= -\frac{\delta \ln \Xi}{\beta \delta[\Psi(\mathbf{r}) - \mu]}. \end{aligned} \quad \text{. . . . . (A-4)}$$

The grand potential Ω is defined by

$$\Omega[\rho(\mathbf{r})] = F[\rho(\mathbf{r})] + \int \mathrm{d}\mathbf{r} \rho(\mathbf{r}) [\Psi(\mathbf{r}) - \mu], \quad \text{. . . . . (A-5)}$$

where F is the intrinsic Helmholtz energy. The relation between Ω and Ξ is given by $\beta\Omega = -\ln\Xi$, which yields $\rho(\mathbf{r}) = \frac{\delta\Omega}{\delta[\Psi(\mathbf{r}) - \mu]}$. At equilibrium, the second law of thermodynamics requires Ω to reach the minimum and $\rho(\mathbf{r})$ must satisfy the condition

$$\frac{\delta\Omega}{\delta\rho(\mathbf{r})} = 0, \text{ or } \frac{\delta F}{\delta\rho(\mathbf{r})} + \Psi(\mathbf{r}) = \mu. \quad \text{. . . . . (A-6)}$$

If an expression for $F[\rho(\mathbf{r})]$ is provided, Eq. A-6 can be used to solve for $\rho(\mathbf{r})$ and subsequently both structural and thermodynamic properties of the system. $F[\rho(\mathbf{r})]$ is typically divided into an ideal term and an excess term. The former is known exactly; it corresponds to the contribution from ideal gas without any intermolecular interactions. The latter has to be formulated by adopting efficient approximations; it accounts for different intermolecular interactions, including short-range repulsion, van der Waals attraction, chemical association, and electrostatic force. The design of the excess Helmholtz energy functional depends on specific requirements, and the numerical performance has to be calibrated by direct comparison with experimental data or molecular simulation results. The detailed formulation of DFT is described by Wu (2006), Wu and Li (2007), Evans (1996), and Wu (2009).

Zhidong Li is a research engineer at ExxonMobil. Previously he was a post-doctoral researcher at RERI. His research interests include thermodynamics of integrated oil recovery/enhanced oil recovery in gas/water injection, asphaltene precipitation and stabilization, shale gas/oil, multiphase equilibrium computations, and pressure/volume/temperature modeling. Li has

published more than 20 papers in peer-reviewed journals. He holds bachelor's and master's degrees from Tsinghua University, Beijing, and a PhD degree from the University of California-Riverside, all in chemical engineering.

Zhehui Jin is a researcher at RERI. His current research interests include thermodynamics of fluids in nanoporous media and statistical thermodynamic modeling of phase behavior in shale gas reservoirs. Jin holds a bachelor's degree in materials science from Tsinghua University and a PhD degree in chemical engineering from University of California-Riverside.

Abbas Firoozabadi is director of RERI and a professor at Yale University. His main research interests are in bulk-phase, irreversible and interfacial thermodynamics; molecular modeling; and physics and mathematics of hydrocarbon reservoirs and production. Firoozabadi's honors and awards include the SPE Anthony Lucas Gold Medal and membership in the US National Academy of Engineering. He holds a bachelor's degree from Abadan Institute of Technology, Iran, and master's and PhD degrees from Illinois Institute of Technology, Chicago, all in natural-gas engineering.